12-2018

Instrumentation-level Improvements in Shear-force Near-field Acoustic Microscopy

J. Bai
Portland State University

P. Devulapalli
Portland State University

Theodore Brockman
Portland State University

Andres H. La Rosa
Portland State University, andres@pdx.edu

Citation Details

Bai, J., Devulapalli, P., Brockman, T., & La Rosa, A. H. (2018, December). Instrumentation-level improvements in shear-force near-field acoustic microscopy. In Journal of Physics: Conference Series (Vol. 1143, No. 1, p. 012013). IOP Publishing.

Instrumentation-level improvements in shear-force near-field acoustic microscopy

IOP Conf. Series: Journal of Physics: Conf. Series **1143** (2018) 012013 doi:10.1088/1742-6596/1143/1/012013

Instrumentation-level improvements in shear-force near-field acoustic microscopy

J Bai, P Devulapalli, T Brockman and Andres H La Rosa
Portland State University, Portland, Oregon 97201, USA

E-mail: bai@pdx.edu

Abstract. The recently introduced Shear-force Near-field Acoustic Microscopy (SANM) brings a new sensing mechanism to the scanning probe microscopy family. SANM's ability to simultaneously monitor, in real time, several physical sample's responses presents some challenges for ensuring optimal operation; namely, avoid "cross-talk" among the multiple signals, address the compensation of thermal drift to ensure reproducibility of the measurements, and measuring the typical low-level signals obtained from nanometer-sized tested regions. Here, several improvements relevant to SANM, but valid for SPM in general, are addressed. *i*) The probe's coarse approach is performed via stepper motors, which are controlled either by a computer software interface, or simply by a user-friendly RF remote control. *ii*) The inherent mechanical drift of the stage is evaluated first (by monitoring the feedback voltage that acts on the sample to maintain the probe-sample distance constant), and then automatically compensated (via linear interpolation) in the immediate subsequent probe's approach/retraction measurements. *iii*) To determine the absolute position of the substrate relative to the probe, the probe-substrate contact current is measured with circuitry properly shielded from eventual electrical ground loops. Buffer amplifiers are used to drive the quartz tuning fork (that holds the probe) and to measure the AC and DC tunneling currents between the tip and sample. *iv*) To improve the signal to noise ratio, a Kalman filter is implemented into the SANM's field-programmable gate array board, which processes the signals in real time. Finally, *v*) to simplify the operation of the microscope, an intuitive LabVIEW host program is developed to control the whole system and offer the user a visualization of the data in real time.

1. Introduction

Shear-force Near-field Acoustic Microscopy (SANM) has recently been introduced as a supportive analytical tool to investigate the viscoelastic properties of mesoscopic fluids trapped between two solid substrates under relative shear motion [1]. SANM joins the family of scanning probe microscopy by bringing near-field acoustic sensing to interrogate such challenging fluid systems. New sensing mechanisms are indeed pertinent in this field since, as it turns out, understanding the striking properties that mesoscopic fluids display when placed under confinement remain as major challenges in condensed matter physics [2], [3]. Some of these properties, quite different from the bulk, include enhanced shear viscosity, prolonged relaxation time, ice formation at room temperature, and hydrophobic interaction range well beyond

commonly accepted molecular interactions ranges. In addition to their fundamental physics interest, an understanding of these properties is also relevant to technological areas like adhesion, wetting processes, and nanotribology [4], [5] (including finding ways to reduce corrosion and wear [6], [7].) It will also have an impact on attaining correct interpretation of high-resolution images acquired by scanning probe microscopy (SPM). The reason lies in the fact that, in SPM, the topography of the surface is inferred from the assumed shear-force interactions [8], [9], the latter comprising the participation of *i*) the SPM probe, *ii*) the interrogated substrate, and *iii*) the mesoscopic fluid trapped in between. It is possible that, in some cases, the features captured in an SPM image are not actual topographic signatures of the substrate, but rather artifacts produced by the different local wetting properties (adsorption, hydrophobicity) of the substrate's surface. In the spirit, then, of providing a reliable metrology tool to characterize solid-fluid interfaces, here we describe few improvements recently incorporated into the SANM, which can be extrapolated to any SPM in general.

2. SANM experimental setup

Figure 1a shows schematically a water meniscus that forms when a solid probe (laterally oscillating at ~ 32 kHz with an amplitude of few nanometers) and a solid substrate are brought in close proximity (~ 20 nm) at ambient conditions. The mesoscopic fluid *i*) affects the lateral motion of the probe, and *ii*) engenders an acoustic wave. The SANM is used to investigate correlations between these two signals and extract from them the elastic and damping properties (k, γ) of the fluid.

Figure 1b shows three distinct sections of the experimental arrangement: *i*) The central part displays a tapered probe attached to one of the tines of a quartz tuning fork (QTF), and a sample (referred here as a metal substrate with its naturally adsorbed—and few monolayer thick—fluid, at ambient conditions. *ii*) The upper part shows a synchronous detection for monitoring the QTF signal, which indicates the probe's lateral oscillation amplitude. *iii*) The bottom side shows an acoustic transducer in intimate contact with the substrate (typically a 2 mm thick piece of glass or silicon wafer), which synchronously senses the near-field acoustic waves engendered at the trapped fluid. At 32 kHz operating frequency, the wavelength of sound in bulk water is ~ 5 cm. For comparison, this acoustic wavelength is much greater than the distance at which the acoustic transducer is placed relative to the mesoscopic fluid in our case; that is, we are detecting the acoustic excitation in the *near field* region from the source.

Figure 1c shows a typical experimental result obtained in the SANM. The probe is initially positioned far away from the substrate and driven at its resonance frequency (~ 32 kHz) and 15 nm initial oscillation amplitude. As the probe approaches the surface (at a rate of 1.5 nm/s) the QTF-signal initially does not change. But at a given distance (which varies stochastically from trial to trial) a water bridge forms between the probe's apex and the substrate, causing the QTF signal to gradually decrease. By about the same time, an acoustic wave is also engendered at the coalesced fluid meniscus, which couples to the substrate and propagates downwards towards the acoustic transducer (SE32-Q, Score Atlanta Inc.) The transducer's signal is synchronously detected with the lock-in amplifier #2; the output of this second lock-in is referred to as the "*acoustic-signal*". By the end of the approach the acoustic signal decreases, which may be the result (among other possibilities that will be addresses elsewhere) that the trapped fluid is quizzed out; that is, the lower the fluid volume, the lower the acoustic signal.

The stochastic nature of the meniscus formation makes each approach/retraction measurement different. Still, some variations may be due to unwanted perturbation from the user (if the measurements are not automated), or by the natural thermal drift (due to the geometrical asymmetries of different parts comprising the microscope stage), or because the noise level is in excess to discriminate the potentially different dynamic response from the tiny volumes (10^{-9} nano-liters) of fluid. These aspects are addressed below, leading to an improvement in the detection of the signals in the SANM.

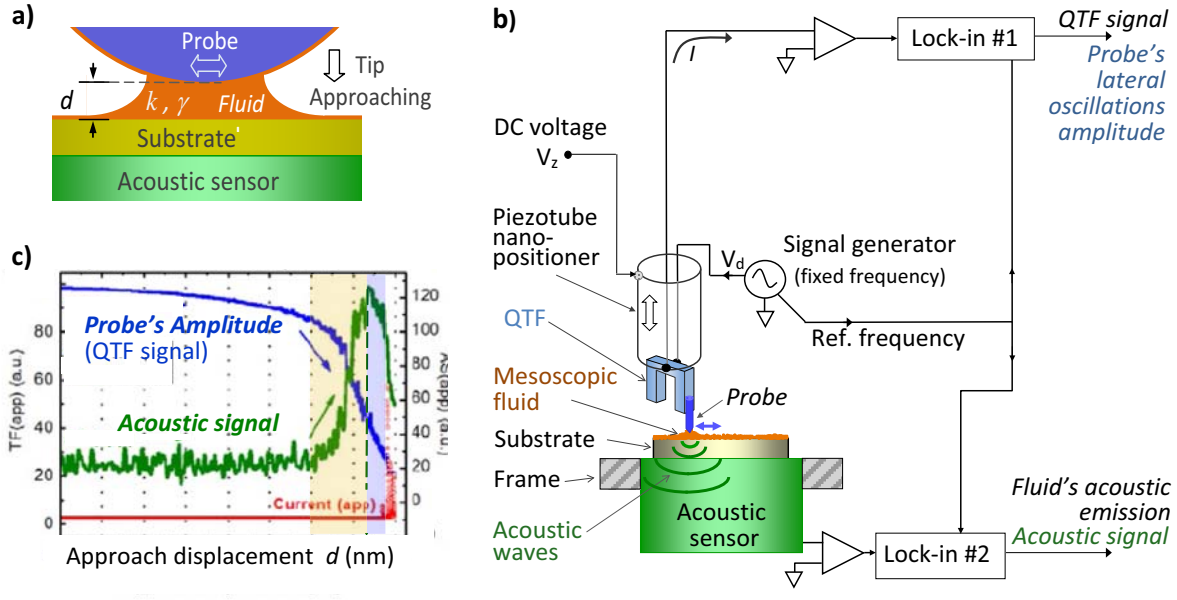

Figure 1. a) Illustration of the mesoscopic fluid (meniscus), confined in the vertical direction by two solid surfaces under shear motion, studied with the SANM. **b**) Schematic experimental setup of the SANM. The probe's lateral oscillations amplitude and the acoustic emission form the mesoscopic fluid are synchronously and simultaneously detected. **c**) Typical variation of the probe's amplitude (blue trace) and acoustic (green trace) signals as the probe approaches the sample. For cases where the probe and the substrate are electrically conductive, the red trace tracks the electrical current that onsets when the probe's apex gets in contact with the substrate. The ability to detect acoustic waves even when the probe is not in mechanical contact with the substrate (*i.e.* sound is engendered at the mesoscopic fluid) constitutes one of the main features of the SANM.

3. The mechanical motion controller of the head stage

During the SANM operation it is typically observed that the probe-sample distance at which a water bridge forms is influenced by the environmental humidity, and that the experimental results are more reproducible at relative humidity greater than 50%. Hence a humidity chamber able to maintain a stable humidity becomes necessary (see Figure 2). But the enclosure obviously imposes access limitations to manually operate the coarse approach of the stage, which is typically implemented by gradually turning three supporting fine screws. To overcome this obstacle, we have implemented a remote control system that operates the screws by activating their corresponding stepper motors. Approaching speed and steps of different approach resolution are available to the user. The implementation is detailed next.

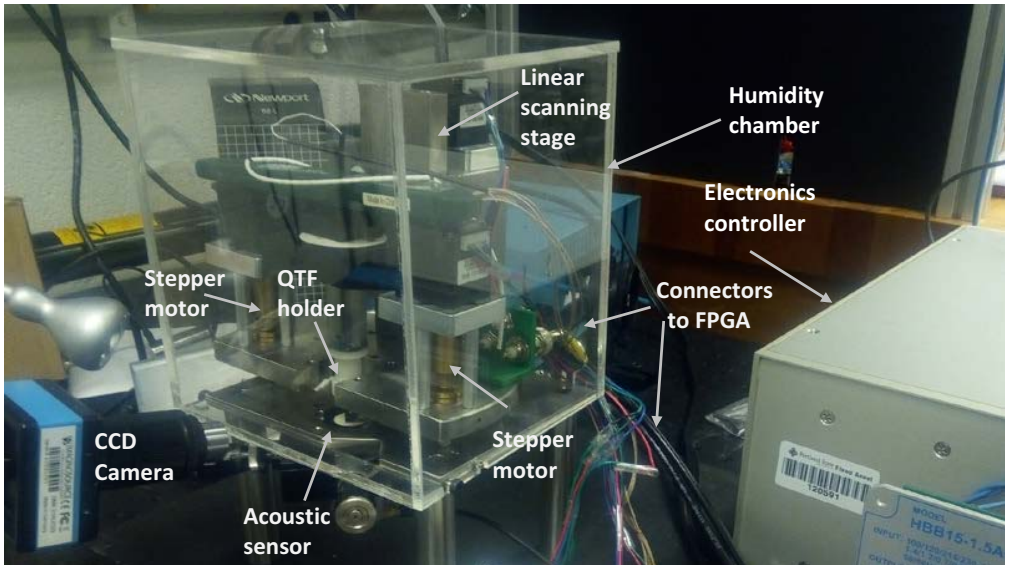

Figure 2. Front side view of the shear-force acoustic near-field microscope.

3.1 Hardware of the stepper motor controller.

A low-cost alternative comprises building the control circuit on a protoboard with three A4988 motor driver boards, and one 315 MHz RF module for portability and accessibility purposses (Figure 3.) Coupling and protection circuits are also built to ensure that the motors run smoothly, quietly, and without skidding or lossing steps. Finally, the motor drive circuit is mounted on an Arduino microcontroller board.

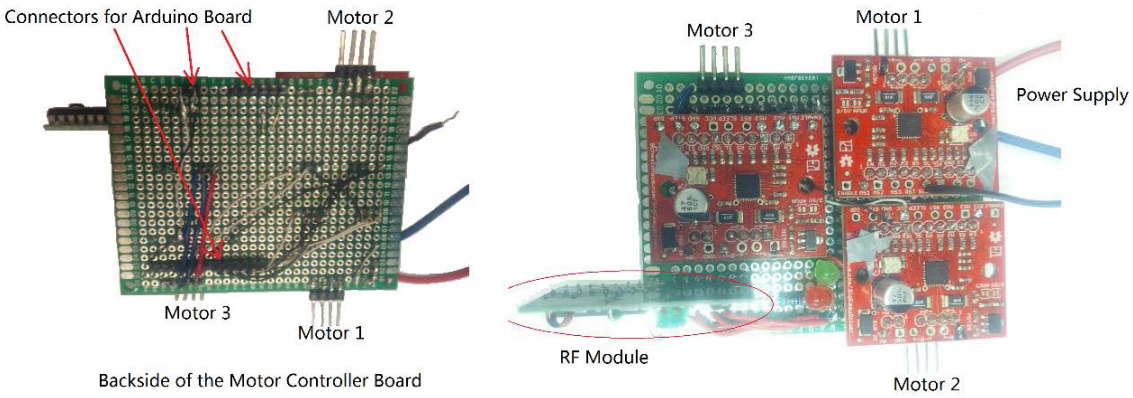

Figure 3. Hardware circuit for controlling the stepper motors.

The inputs of the A4988 driver boards are connected to pins 2 to 13 of the Arduino board. The RF module is connected to pins A0 to A3 of the Arduino board. Pins A4 and A5 of the Arduino board are connected to 2 LEDs for display purposes (Figure 4). More details can be found in the spec of the A4988 chip [10]. The RF module is paired with a four-button remote controller unit. Usually, when one button is

pressed, one line of the RF module will be pulled to High. The mapping between the controller's buttons, the RF data lines, and the Arduino pins should be carefully verified. Figure 5 shows the mapping selected for the current implementation.

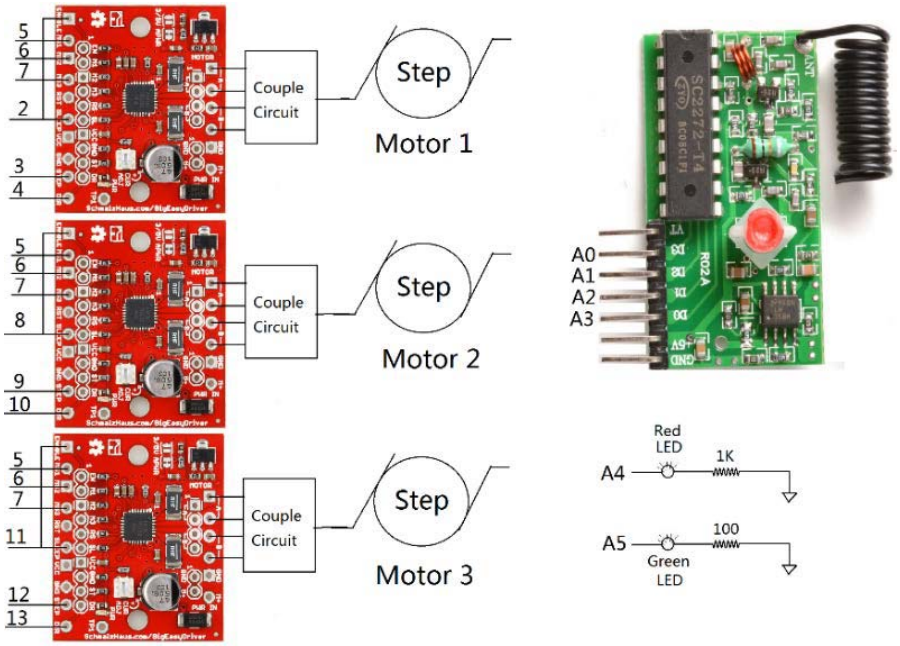

Figure 4. Electric connections of the modules. The left side shows the three A4988 driver boards; the right side shows the RF module.

Controller	A	B	C	D
RF Module	D2	D0	D3	D1
Arduino	A1	A3	A0	A2

Figure 5. The 4-button remote controller and mapping of its buttons to the Arduino pins.

3.2 The logic structure of the mechanical motion controller

A 3-layer model would be sufficient to model this motor controller. But, for future integration purposes involving a larger project, we have built the system with a 4-layer model. Accordingly, the test applications are on the fourth layer, while the stage motion functions are on the third layer. The instructions to control the specific motion of each motor are located on the second layer. The first layer is the relevant hardware. The final structure of the controller is shown in table 1. The benefits of a 4-layer model include better

hardware compatibility, easier programming on each abstract level, and flexibility in software updating and maintenance [11], [12].

Table 1. 4-layer model for the mechanical motion controller

Abstract Level	Description	Targets
Layer 4	Apication Layer	Running on PC
Layer 3	Functional Block	Running on PC
Layer 2	Instructions	Arduino
Layer 1	Hardware	Arduino, Analog and Digital Circuits

3.3 Layer 2 description of the mechanical controller.

Table 2 shows the detailed components of the mechanical controller on each layer. Layer 2 of the system is implemented in an Arduino UNO microcontroller board. The *RF Signal Decoding Module* builds a transparent bridge between button actions of the RF remote and the Arduino instructions. The *RF Signal Decoding Module* will interpret the button pushing actions as different commands sending to the Arduino board. Human behaviors and reactions are integrated into the module already. This makes the RF control more intuitive.

Table 2. Modules of the mechanical controller.

Abstract Level	Hardware and Software Resources
Layer 4	Applications
Layer 3	LabVIEW FSM Controlling Stage Motions, Human Controlling the RF Remote
Layer 2	RF Signal Decoding Module, A4988 Encoding Module, Stage Action Module, Communication FSM
Layer 1	A4988 Motor Driver Boards, RF Receiver Module, LEDs, Arduino Board, 4 Button RF Remote

The *A4988 Module* masks the detailed signal waveforms of the motor controllers. It receives commands from the *Stage Action Module* and controls the actual movement of the motors. The *Stage Action Module* controls the head stage to move down or up, fast or slow, as well as continuously or by one step at a time.

The *Communication Finite State Machine* (FSM) is the interface between the Arduino board and the outside world. The FSM is continuously running in a loop, taking commands from the third layer of the system and passing them to the *Stage Action Module*. Figure 8 shows the state diagram of the FSM. The default mode of the FSM is *Computer Control*, where the FSM reads commands from the third layer program running on a computer. In RF mode, the FSM receives signals from an RF remote and does various actions depending on the RF signal sequences. See figure 6.

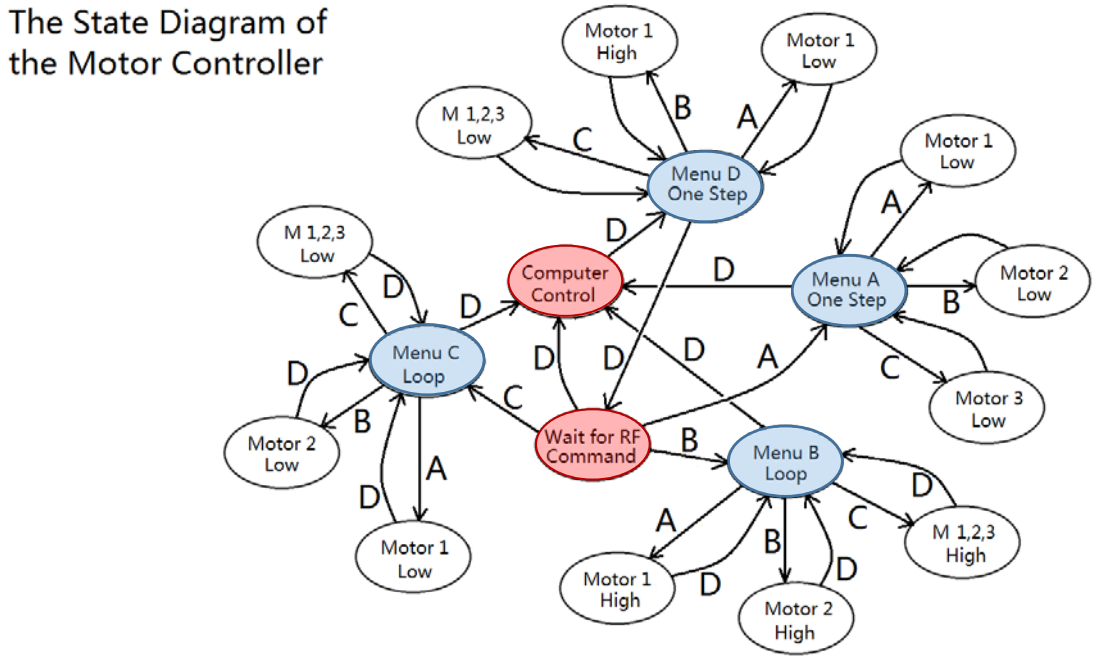

Figure 6. State diagram of the *Communication Finite State Machine* (FSM) running on an Arduino microcontroller.

The FSM is the interface between the Arduino microcontroller, the third layer program, and the RF remote. For simplicity, the LED display actions are not shown in Figure 6. The default state of the FSM is *Computer Control*. *i*) When button *D* is pressed, the controller enters into *Menu D*, which is the default RF state. Pressing buttons A, *B* or *C* will trigger 3 actions (see the state diagram). When button *D* is pressed again, the controller will leave the default RF state and enter into the menu selection state, *Wait for RF Command*. Then, pressing buttons A, *B* or *C* will drive the controller into *Menu A, Menu B*, or *Menu C,* respectively. *ii*) Menu A is a one-step function menu, where each function will only execute once upon receiving an RF signal. *iii*) *Menu B* and *Menu C* are continuous function menus, where the function will execute continuously until a button *D* signal arrives. *iv*) While in *Menu A, B, C* or *D*, one more push of button *D* will drive the controller back to *Computer Control* state. During all the transitions, two LEDs will indicate the state of the controller in real time.

The FSM also controls two 5-state LEDs to indicate the current state of the FSM. The 5 states of the LEDs are *ON*, *OFF, BLINKING, FLASHING*, and *DIM* (see table 3). Combining the two LEDs, one can obtain 10 to 25 state capacity. This capability would be very convenient in cases where the stage is in, for example, a vacuum chamber or other enclosed environment, and therefore the operator cannot see the movement of the stage. In those cases, the LED state indicators will show the users the hidden motion of the stage.

When the FSM is in the *Computer Control* state, it uses a 3-byte array to communicate with the computer. Every time the FSM reads 3 bytes of string from the computer, it will verify the first 2 bytes. If the first 2 bytes are character “L” and “C”, the third byte will be decoded. Based on the decoding results, various functions will be called to carry out the corresponding operations. Communication via formatted strings helps reduce the error during data transfer. Strategies to format the control commands can be found in the references [11].

Table 3. The 5 state display scheme of the LED indicators.

LED States	FSM States
Green ON	Computer Control
Red ON	Menu D
OFF	Menu Select
Dim	Functions Are Running
Blink	Menu A, B, or C
Flash	Stop, Quit

3.4 Layer 3 description of the mechanical controller.
The layer 3 program runs on the host computer (PC). An example of layer 3 is shown in figure 7. Six latch buttons control the vertical motion of the stage. When they are pressed (released) the stage will move (stop) accordingly. M1, M2, and M3 are used to control the 3 motors to move with one step, during the final approach. The one-step mechanical motion of the stage has a resolution of about 650 nm.

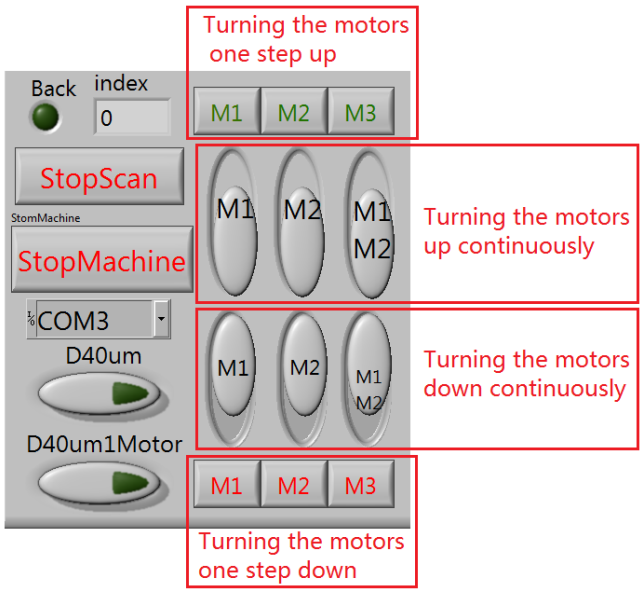

Figure 7. User-interface for controlling the motion of the SANM head-stage.

The Layer 3 program is also coded as an FSM (a section of the LabVIEW code is shown in figure 8.) An attractive feature of this programming method is that Layer 3 and Layer 2 can work at their own speed, and interact with each other asynchronously, which greatly simplifies the programming efforts and enables the

whole system to be more stable and reliable. The methods about how to coordinate the functions running on layer 2 and layer 3 are covered in the references [11] and [13].

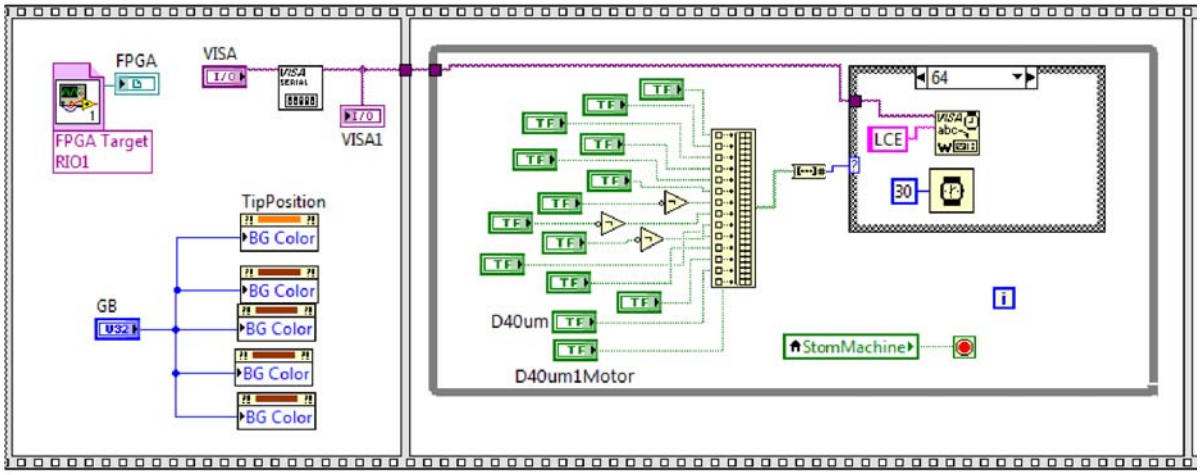

Figure 8. A section of the LabVIEW block diagram for controlling the head stage motion (running on layer 3 of the mechanical controller), coded according to the FSM displayed in figure 6. Motion actions are represented with Boolean buttons, which are built into a vector to control the execution of the FSM. States of the FSM are coded with LabVIEW case structures.

4. Compensation of the thermal drift

Mechanical drift is a problem in scanning acoustic microscopy. Due to ambient temperature variations, mechanical structures are subjected to expansions or contractions. The size of different sections of the microscope's head-stage, in particular, may vary differently (due to their asymmetric geometries), which introduces uncertainty to the actual location of the analyzed sample surface. This is referred to as the thermal drift to the system. In order to have an accurate measurement of the actual (and no juts relative) distance between the tip and the sample, this drift must be compensated. Our approach is outlined in figures 9 and 10. Figure 9 outlines the system used to perform the approach of the tip to the sample: *i*) a coarse approach, using screws controlled by stepper motors (as described in the previous section), followed by *ii*) a fine approach, using a high-voltage controlled piezoelectric linear stage (Mad City Labs, OP65; 60 microns travel range.) Then the probe is engaged into feedback with the sample, which maintains the probe-sample distance constant.

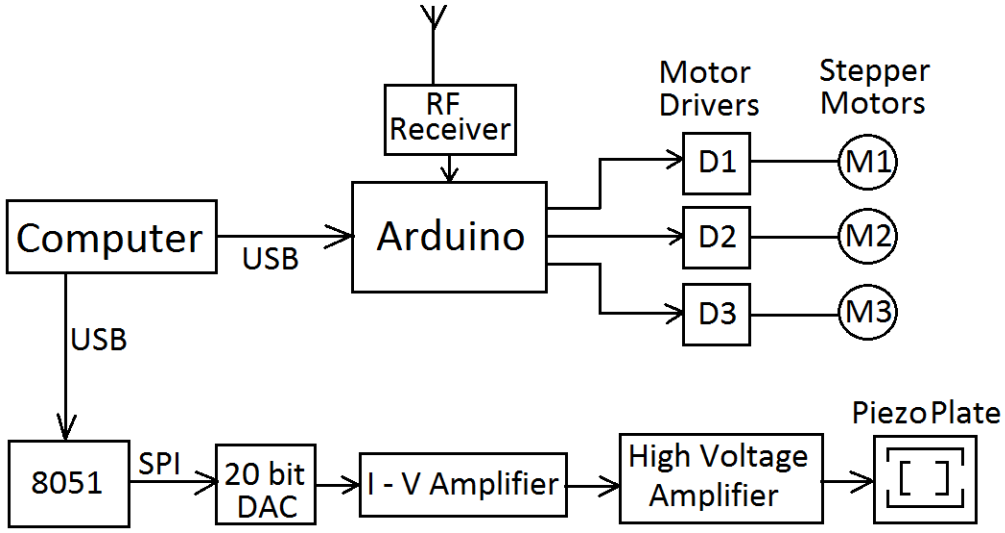

Figure 9. Signal flow graph of the coarse (top) and fine (bottom) motion control mechanism.

Figure 10 outlines the thermal drift compensation scheme. While the probe and sample are engaged in feedback, the thermal drift is evaluated by monitoring the output feedback voltage needed to keep the probe-sample distance constant. In our system, the probe is held by the piezoelectric linear stage, and the sample rests on a nominally fixed position stage. The sensing signal is provided by the QTF response (the probe's lateral oscillations amplitude) and the corresponding corrected output voltage is applied to the piezoelectric stage.

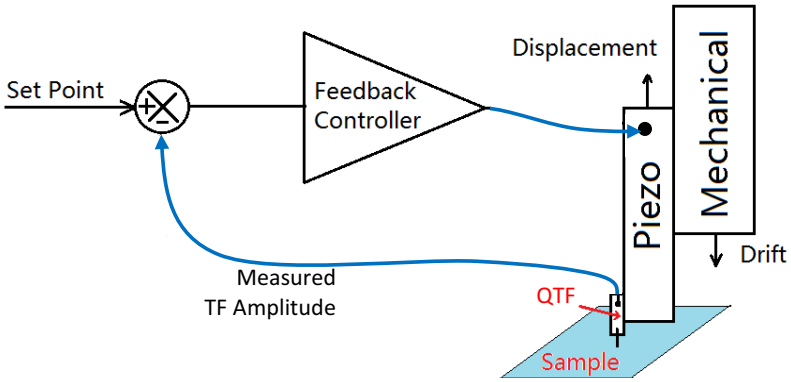

Figure 10. Illustration of the drift measurement scheme. A PID feedback controller is used to first measure the mechanical drift of the sample stage relative to the head stage. The QTF signal (that monitors the probe's amplitude of oscillations) is selected as the control variable of the feedback controller. After the tip is engaged to the sample surface, the voltage feedback control allows to measure the drift. This information is then read by the microscope controller to take it into account in the subsequent approach/retraction measurement. All this process is automated.

Recapitulating: *i*) One starts lowering the scanning stage at coarse steps, via the activation of stepper-motors, followed by a piezoelectric fine approach. *ii*) Subsequently, the tip is engaged in feedback with the sample surface. To avoid probe's damage, a conservative set point of 80% of the free run TF amplitude is selected; then the feedback controller strives to maintain the TF amplitude constant by continuously applying a correction voltage. *iii*) Suppose the mechanical structure holding the sample were drifting down; then a voltage feedback will drive the top stage down to maintain a constant probe-sample distance (see figure 10). *iv*) The piezo displacements (drift compensation data) are recorded, linearly interpolated; this added drift information is incorporated into the piezo driver that is programmed for the subsequent probe approach process. We assume the system drift would be the same during a short period of time an approach/retraction process takes place (~30 seconds). *v*) In our current system, this drift compensation scheme is integrated into the main controller. Every time, before an approaching and retraction process, the system measures the drift automatically and compensate the drift for the next approaching/ retraction process.

5. Monitoring probe-sample contact current

The strategy followed in the SANM—using a probe that successively approaches and retracts from the substrate as a way to interrogate the liquid-solid interface—places on a preponderant status the need to locate with precision the location of the surface relative to the probe. The drift compensation addressed above, ensuring an accurate probe-sample distance control, is a good step. But to obtain the absolute distance between the tip and the sample surface it is necessary to locate the point at which the probe encounters the substrate. Here we establish that point by monitoring the contact current. We apply a bias voltage to the tip and measure the ac-component of the tunneling current synchronously with a lock-in amplifier and the dc-component with a buffer amplifier (Figure 11). When a metal tip touches the metallic substrate, the current passing through the substrate should grow exponentially.

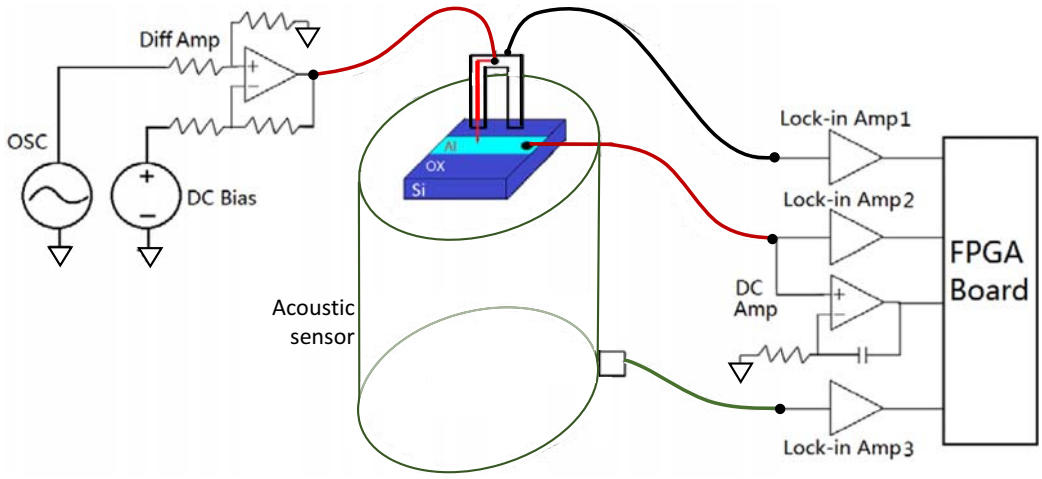

Figure 11. Experimental setup for measuring the probe-sample contact current, and avoid electrical interference with the simultaneously measured QTF signal (with lock-in #1) and the acoustic signal (lock-in #3).

The multiple signals monitored simultaneously in the SANM makes also imperative to put electrical guards against potential "crosstalk" among the signals. Figure 11 shows the experimental setting aiming at fulfilling that objective; Figure 12 shows the corresponding circuit diagram. The left side of Figure 11 shows how we use a differential amplifier to drive the QTF. An AC voltage (~ mV amplitude) is connected to the positive input of the OpAmp. A DC bias voltage is connected to the negative input of the OpAmp. Because the OpAmp has a very large input impedance (~ 10^6 Ω), the AC and DC signal sources are practically isolated. This way the potential difference between the tip and the sample can be safely be controlled with the DC signal. At the right side, three lock-in amplifiers are used to independently measure the QTF, acoustic SANM, and AC tunneling current signals. Notice the additional buffer amplifier to measure the DC tunneling current. The buffer is configured as an integrator; by choosing a proper value of the capacitor the ac-components of the tunneling current signal is filtered by the integrator, and only its DC component is picked up by the buffer amplifier. It is worth highlighting also that the buffer amplifier establishes a virtual ground to the sample. This virtual ground at the sample (introduced by the buffer amplifier) and the input bias voltage (provided by the differential amplifier) stablishes the bias between the tip and sample. This biasing mechanism adds confidence to the control and monitoring of the signals. Because the OpAmp has a very large input impedance, the buffer amplifier will not leak the high-frequency tunneling signal away. Then both AC and DC tunneling signals can be measured accurately. Figure 13 shows typically measured curves of the QTF, acoustic and tunneling current during an approaching process.

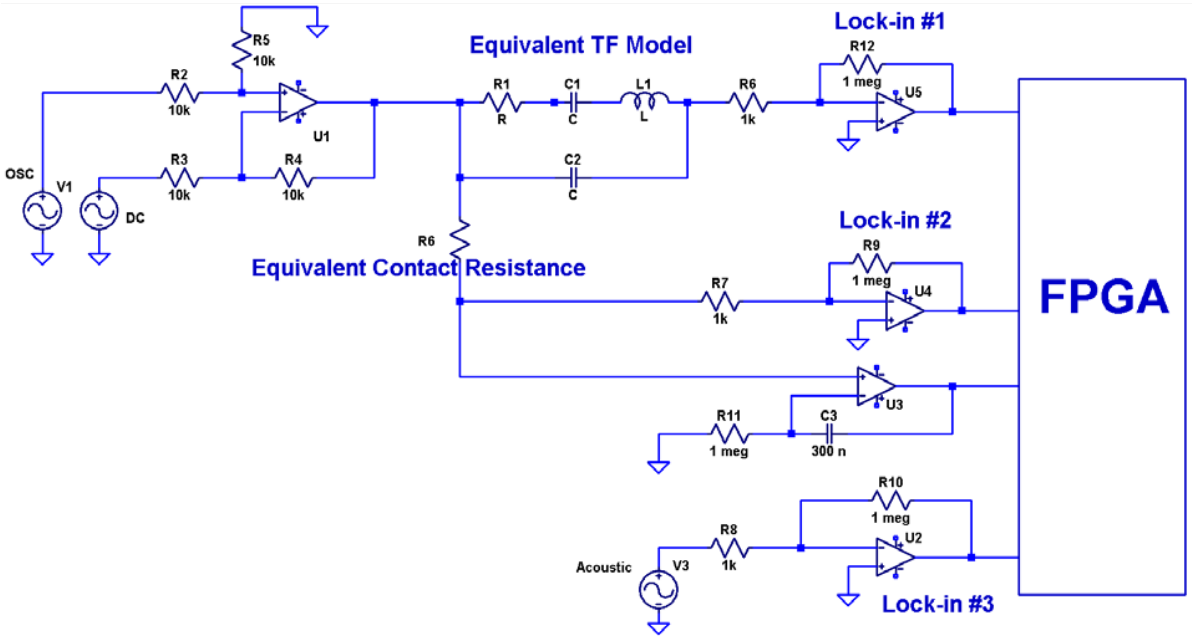

Figure 12. Circuit diagram for monitoring the probe's lateral oscillations amplitude (QTF signal, top lock-in #1), fluid's acoustic emission signal (bottom lock-in #3), and the probe-sample ac/dc contact current (lock-in #2 and buffer circuit) in the SANM. R6 is the equivalent resistance between the tip and the sample. Lock-in #1, Lock-in #2 and Lock-in #3 are the equivalent input circuits of the lock-in amplifiers when they are configured as current input with a 1kΩ virtual impedance to ground. R11 can

be selected from 1kΩ to 1MΩ, since the attenuation of the 32 kHz signal varies from -35dB to -95dB. If we were to set the high frequency attenuation to be -40dB, then R11 should be 2 k Ω.

Figure 13. Typical approach curves measured in the SANM. Notice, some current is measured through the fluid bridge prior to the state where the probe encounters the solid substrate. The latter is identified when the current drastically increases.

6. Real-time signal processing with a Kalman filter

At this stage, the detection of the acoustic SANM signal has not been fully optimized yet. Due to the stochastic nature of the tip and fluid interaction, a Kalman filter is implemented into the FPGA board to obtain optimal filtered measurements in real time. Implementation of Kalman filter requires a system process model and a measurement model of the system being masured [14].

6.1 The system process model

Since the QTF and the acoustic are the major signals used in the SANM, we define the state vectors x as follows,

$$x = \begin{bmatrix} A_{TF} \\ A_{AC} \end{bmatrix} \tag{1}$$

where A_{TF} is the amplitude of the QTF signal, and A_{AC} is the amplitude of the acoustic signal. Since, experimentally, the QTF is excited by an external voltage, the tuning fork signal A_{TF} will be modeled as a random walk. Prior experiments indicates a correlation between the acoustic response and the QTF oscillations amplitude; hence we model the acoustic signal A_{AC} also as a random walk.

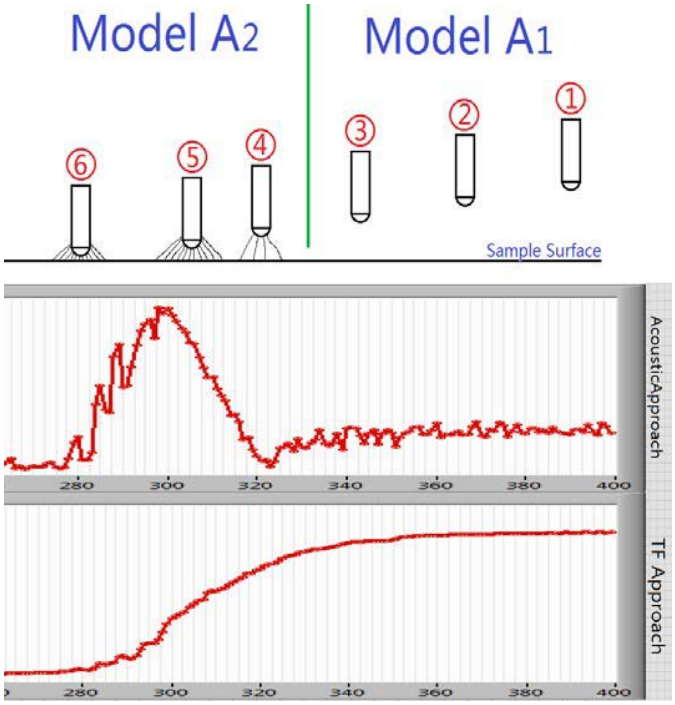

Figure 14. The QTF and acoustic signal profiles are used to build the process models. In Model A1, the tip is far away from the sample surface; hence there is no interaction between them. Both signals are modeled with a random walk. Model A2 incorporates information that a fluid bridge builds up between the tip and the sample surface at a stochastic probe-sample distance during the approach. Then the vibration of the tip is propagating through the bridge to the sample. The acoustic signal is modeled as a random walk with a small linear influence from the QTF. The figures show the results of a probe to sample approach; the filtering process was applied in real-time.

Let's start with the tip at position 1 (see Figure 14). Then the process model of the system is:

$$x_{n+1} = A_1 x_n + w_n \tag{2}$$

$$A_1 = \begin{bmatrix} 0.98 & 0 \\ 0 & 0.98 \end{bmatrix} \tag{3}$$

where A_1 embodies the random walk model; x_n is the state at time-step n, and w_n is the process noise at the time-step n.

After the tip makes a contact with the fluid layer, we model the acoustic signal with an inertial function lumped by a linear function of the QTF signal. This springs from the fact that in previous experiments it has been verified that the acoustic signal is proportional to the QTF amplitude [15]. On a first-order

approximation, the acoustic signal is modeled as, $A_{AC_{n+1}} = 2\alpha\, A_{TF_n} + A_{AC_n}$, where the coefficient α is a relative small number. As a first order approximation, α represents the linear corelation between the QTF oscillation and the acoustic signal strength. For different lab setups, this corelation may vary. So after many lab trials, α needs to be set very carefully to have the best fitlter effects. After hundereds of trials and comparisons, α will be set automatically by an algorithm. Then the process model becomes:

$$x_{n+1} = A_2 x_n + w_n \tag{4}$$

$$A_2 = \begin{bmatrix} 0.98 & 0 \\ 2\alpha & 0.98 \end{bmatrix} \tag{5}$$

where A_2 is the process model after a fluid bridge is built between the tip and the sample surface; x_n and w_n are the state and the process noise at time step n is respectively. The time at which model-2 kicks from model-1 is described below.

6.2 The measurement model

Since the QTF and acoustic signals are the ones we want to measure, the following measurement model is used:

$$y_n = C x_n + v_n \tag{6}$$

$$C = \begin{bmatrix} 1 & 0 \\ 0 & 1 \end{bmatrix} \tag{7}$$

where y_n is the measured vector at time step n; C is the measurement matrix, v_n is the measurement noise at time step n.

The Kalman filter is initialized with a direct measurement of x_0, at time step 0. At time step n, the Kalman filter is updated with the sequence shown below [14].

$$\hat{x}_n^- = A_1 \hat{x}_{n-1} \tag{8}$$

$$\hat{x}_n^- = A_2 \hat{x}_{n-1} \tag{8b}$$

$$P_n^- = A_1 P_{n-1} A_1^T + Q_{n-1} \tag{9}$$

$$P_n^- = A_2 P_{n-1} A_2^T + Q_{n-1} \tag{9b}$$

$$K_n = \frac{P_n^- C^T}{C P_n^- C^T + R_n} \tag{10}$$

$$e_n = (y_n - C\hat{x}_n^-) \tag{11}$$

$$\hat{x}_n = \hat{x}_n^- + K_n e_n \tag{12}$$

$$P_n = (I - K_n C) P_n^- \tag{13}$$

where $\hat{x}_n^-$ is the estimated state before a measurement is taken at the time step n; P_n^- is the state covariance before a measurement is taken at the time step n; K_n is the Kalman gain at the time step n; $\hat{x}_n$ is the state

estimate after a measurement is taken at the time step n; P_n is the state covariance after a measurement is taken at the time step n.

A threshold was set up to monitor the values of e_n in 5 steps. According to different value history of e_n , the system may switch between models A_1 and A_2. In model A_2, equations (8b) and (9b) would be used to update the system. The Kalman filter was implemented in the FPGA board, parameters Q_n and R_n are the process covariance and measurement covariance, respectively. For different setups, Q_n and R_n should be carefully chosen and tuned. Figure 15 shows acoustic signals acquired with and without a filtering process.

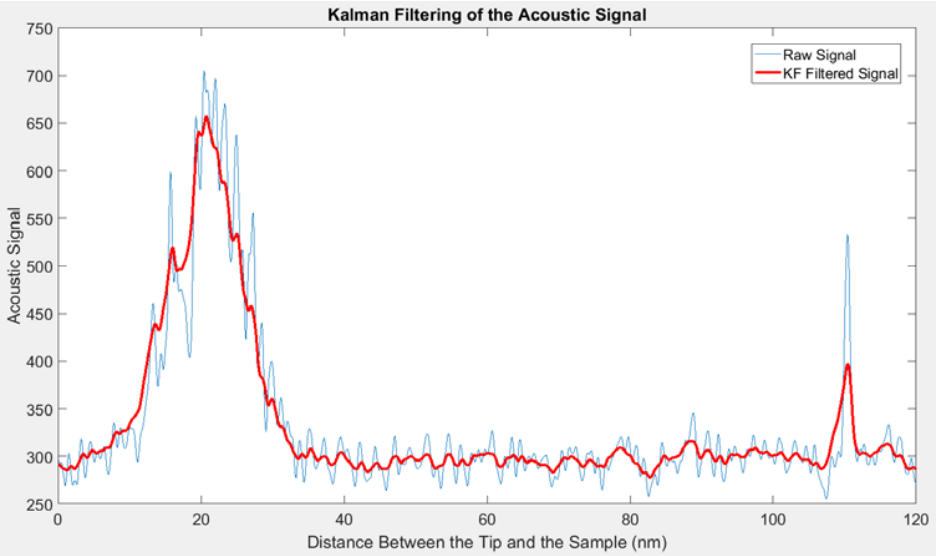

Figure 15. A comparison between acoustic traces logged without the filter in place (blue trace) and with the real-time filter in place (red trace).

The information of the SANM from previous measurements makes the user know more about the experiments and the instrument; wqith this information, one generates a simple linear model. As shown in Fig. 5, a simple model improves the signal quality significantly already. With a more accurate model better results can be achieved, by using, for example an Unscented Kalman filter (UKF).

Since the Kalman filter offers the optimal estimates of the measured signals, in the future we plan to use whispering-galley acoustic sensing [16] as an on-line sense signal for a feedback controller. Then an online-filtered acoustic SPM image of the sample can be obtained.

7. The integrated host program

In order to simplify the operation of the SANM microscope, an intuitive host program was developed to control the system resources and display the measured signals. Figure 16 shows the interface of the scanning acoustic microscope host program coded with LabVIEW. At the beginning, the operator clicks the various motor control buttons to lower the stage at coarse steps. The minimum mechanical movement of the stage is about 650 nm. With the aid of a microscope lens attached to a CCD camera (see figure 2), the user is able to monitor the motion of the probe. When the probe is in the proximity of the sample surface, one switches

to finer step approaches with three piezo controlled slides, as shown in figure 16 (the three slides activate the same piezoelectric linear stage.) The piezo is controlled by a 20 bit DAC chip (see figure 9). The total range of the piezo stage is 65 μm. So for a 20 bit DAC, the nominal theoretical resolution is 0.06 nm. Here. the left slide is designed to have 200 nm resolution, the middle slide has 20 nm resolution steps. The right slide has a nominal 0.2 nm resolution, but due to the noise level of the piezo controller and thermal fluctuation of the whole system, the probe may not have a real resolution as fine as indicated on the front panel. For different hardware setup, calibration and testing would be needed. The real-time probe position indicator in the panel shows the relative probe position being driven by the piezo. When the probe is driven by the piezo either manually or automatically, this window will show the trace of the probe.

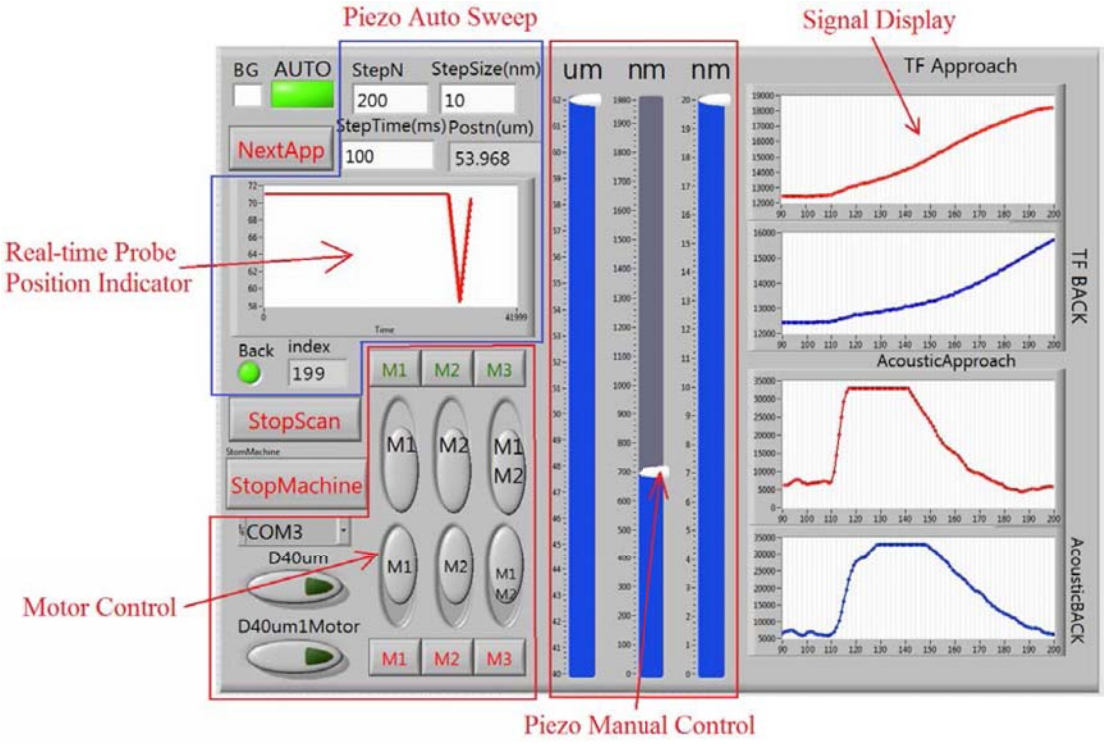

Figure 16. The front panel of the controller.

When the *AUTO* button is hit, the probe will perform an automatic approach and retraction along the Z-axis. *StepN* controls the step number of the approach and retraction curves. *StepTime* controls the time interval of each step. During an automatic approach and retraction, the measured signals will be logged by the FPGA board and showed on the signal display windows.

The *BG* button is used to control the background color. For computer monitoring, one may want a black background; while for printing, one may want a white background.

8. Conclusions

Several instrumentation-level improvements for applications in scanning probe microscopy, in general, and for shear-force near-field acoustic microscopy, in particular, were addressed. The automated coarse

(micrometer-sized steps) and fine (nanometer steps) approach allow minimal interference of the operator on the functioning of the microscope. A friendly graphic user interface allows the operation of the microscope remotely. This feature opens the opportunity to implement, in the near future, operation of the microscope via an internet connection, which would be valuable to establish international collaborations since the microscope could be operated from any place in the world. Another important feature of the new SANM is to be immune to electrical ground loops when monitoring the probe-sample contact current (in addition to the probe's amplitude of lateral oscillations and the acoustic signals.) The circuits that enable this capability were shown explicitly. Finally, a real-time Kalman filtering of the signals was implemented for the first time in the SANM. The effectiveness of the Kalman filter was demonstrated even with a relatively simple linear model. In the near future, real-time Kalman filter implemented with whispering-gallery acoustic sensing signal will be used to feedback-control the tip's movement, which will allow to acquire on-line filtered SPM images can be obtained. All the instrumentation-level improvements introduced in this paper will make the SANM experiments easier to perform, accurate, and more reproducible.

Bibliography

[1] La Rosa A H, R. Nordstrom, Cui X, McCollum J and Li N 2005 The Ultrasonic/Shear-Force Microscope: Integrating Ultrasonic Sensing into NSOM *Rev. Sci. Instrum.* **76** 093707 http://pdxscholar.library.pdx.edu/cgi/viewcontent.cgi?article=1009&context=phy_fac

[2] Kim B, Kwon S, Mun H, An S, Jhe W 2014 Energy dissipation of nanoconfined hydration layer: Long-range hydration on the hydrophilic solid surface *Scientific Reports* **4** 6499

[3] Granick S, Motions and Relaxations of Confined Liquids *Science* **253** 1374

[4] Urbakh, Klafter J M, Gourdon D and Israelachvili J 2004 The nonlinear nature of friction *Nature* 430, 525

[5] Hammer M U, Anderson T H, Chaimovich A, M. Shell S and Israelachvili J 2010 The search for the hydrophobic force law *Faraday Discuss*. **146** 299

[6] N. J. Persson 2000 Sliding Friction (Springer)

[7] Kim S H, Asay D B and Dugger M T 2007 Nanotribology and MEMS *Nano Today* **2** 22

[8] Daniel Courjon 2003 Near-Field Microscopy and Near-Field Optics (Imperial College Press)

[9] Zhang Z, Ahn P, Dong B, Balogu O, Sun C 2013 Quantitative Imaging of Rapidly Decaying Evanescent Fields Using Plasmonic Near-Field Scanning Optical Microscopy *Scientific Reports* **3**, Article number: 2803

[10] Allegro, A4988 DMOS Microstepping Driver with Translator and Overcurrent Protection, http://www.allegromicro.com/en/Products/Motor-Driver-And-Interface-ICs/Bipolar-Stepper-Motor-Drivers/A4aspx

[11] Bai J, La Rosa A H. 2017 Essentials of Building Virtual Instruments with LabVIEW and Arduino for Lab Automation Applications, International Journal of Science and Research (IJSR), https://www.ijsr.net/archive/v6i5/v6i5.php, **6** 640

[12] Bai J, Chen J, Freeouf J, La Rosa A H. A 4-layer method of developing integrated sensor systems with LabVIEW, Journal of Measurement Science and Instrumentation. 10.3969/j.issn.1674-8042.2013.04.001

[13] Bai J, La Rosa A H 2017 An SPM Stage Driven by 3 Stepper Motors. Journal of Measurement Science and Instrumentation. 10.3969/j.issn.1674-8042.2017.03.010

[14] Simon Haykin, Chapter I, Kalman Filters, Kalman Filtering and Neural Networks, Wiley, 2001
[15] Wang X, Fernandez R, Li N, Hung H, Venkataraman A, Nordstrom R, and La Rosa A H 2016 "Near-field acousto monitoring shear interactions inside a drop of fluid: The role of the zero-slip condition." *Physics of Fluids* **28** 052001 doi: 10.1063/1.4947597.
[16] La Rosa A H, Li N, Fernandez R, Wang X, Nordstrom R, and Padigi S K 2011 "Whispering-gallery acoustic sensing: Characterization of mesoscopic films and scanning probe microscopy applications, *Rev. Sci. Instrum*. **82**, 093704